Forecasting of Rock Failure in the Laboratory using Active Acoustic Monitoring Methods

A. Veltmeijer[1], M. Naderloo[1], A. Barnhoorn[1]

[1]Faculty of Civil Engineering & Geosciences, Delft University of Technology, Delft, The Netherlands

Key Points:

- Multiple waveform characteristics are compared for forecasting and monitoring potential of rock failure at different confining pressures
- The upcoming failure of the rock samples can be forecasted from 40 to 70% of its failure point
- A traffic light system using active acoustic monitoring is proposed to forecast and mitigate failure at various depths and stress conditions

Corresponding author: Aukje Veltmeijer, a.v.veltmeijer@tudelft.nl

Abstract

Predicting stress changes in the subsurface leading to failure or seismicity remains challenging. Developing a robust monitoring method can help the prediction and thus mitigation of natural hazards. Ultrasonic transmission experiments were performed on Red Pfaelzer sandstones to investigate the forecasting potential to failure at different confining pressures. The forecasting potential for failure of the energy of the direct and coda wave, the transmissivity, Q-factor, coda wave decorrelation coefficient, and velocity change by coda wave interferometry are investigated and compared. Our results show the failure of the tested samples can be forecasted from 40 to 70% of the failure point. Small differences are visible in the precursors between the tested confining pressures, but as the trends are very similar, a robust prediction of failure can be made by combining the various analyses techniques. In this paper, we propose a traffic light forecasting system using active acoustic monitoring which is applicable for forecasting failure at various depths and or stress conditions, for a better prediction of small stress-induced changes in the subsurface and thus mitigation of failure (and seismicity) in the subsurface.

Plain Language Summary

Forecasting the occurrence of natural hazards, such as earthquakes or landslides, remain very challenging. These hazards are often caused by stress changes in the subsurface, therefore detecting and monitoring these changes can help the prediction and mitigation. Active ultrasonic transmission experiments were performed on Red Pfaelzer sandstones to investigate the monitoring and forecasting potential of these measurements. The sandstone samples were loaded until failure at different initial confining stress conditions. The forecasting potential to failure of different analysis methods is investigated and compared. Our results show we can detect the forecast the upcoming failure of the samples from 40 to 70% of its failure point. Small differences between each analysis method are visible, but the trend of the signal is leading and therefore a robust prediction of failure can be made by combining analysis methods. In this paper, we propose a traffic light forecasting system using active acoustic monitoring which is applicable for forecasting failure at various depths and or stress conditions, for a better prediction of small stress-induced changes in the subsurface and thus mitigation of failure (natural hazards) in the subsurface.

1 Introduction

Natural hazards, such as earthquakes or landslides, can cause much damage. These events often result from precursory stress changes in the medium or along fault zones. Predicting the degree of these stress changes, and as a result, the potential onset and exact location of failure or seismicity remain very challenging.

Therefore, developing a robust method that can monitor these stress changes is crucial for a better prediction and thus mitigation of failure and seismicity in the subsurface. To monitor the physical properties of the subsurface, remotely and non-destructively, geophysical methods can be used. Monitoring the seismic velocities provides insight into mechanical (rigidity, density, etc.) evolution (Schubnel et al., 2006). A number of geomechanical properties influence the propagation of elastic waves through a medium. Structural characteristics, including, rock type, mineralogy, porosity, and fluid type, but also environmental characteristics like effective stress (Hall, 2009), temperature (Snieder et al., 2002), and saturation (Grêt, Snieder, & Scales, 2006) change the elastic moduli and thus influence the propagation (Hall, 2009). The stress changes can be quantified by analyzing the change in acoustic or seismic velocity (Xie et al., 2018). The stress changes in the subsurface can cause micro-crack formation, this crack damage can lead to a decrease in elastic wave velocities, and in the development of anisotropy (Schubnel et al., 2006). However, the sensitivity of seismic wave velocity to stress changes in rocks is low

(Nur, 1971; Grêt, Snieder, & Scales, 2006; Grêt, Snieder, & Özbay, 2006; Barnhoorn et al., 2018) and detection of temporal variations is therefore difficult (Niu et al., 2003; Grêt, Snieder, & Özbay, 2006). By analyzing the direct arrivals, dispersion envelope, the coda wave or attenuation (Q-factor) stress changes in the subsurface can also be monitored (Snieder et al., 2006; Schubnel et al., 2006; Grêt, Snieder, & Scales, 2006; Grêt, Snieder, & Özbay, 2006; Hall, 2009; Barnhoorn et al., 2018; Xie et al., 2018).

The coda wave can be used to monitor small changes in a medium, it scatters throughout the rock and samples a disturbed region more than a direct wave (Snieder, 2006). Therefore, small changes, like micro-crack damage, which may be undetectable in direct waves, are amplified by repeated sampling and detected by the coda. Coda waves are used in many applications, such as monitoring of fault zones (Poupinet et al., 1984; Niu et al., 2008), volcano's (Grêt et al., 2005; Snieder et al., 2006), the integrity of concrete (Deroo et al., 2010; Niederleithinger et al., 2018), temporal changes in the subsurface and in-situ stress (Grêt, Snieder, & Scales, 2006; Grêt, Snieder, & Özbay, 2006), or to monitor velocity changes in laboratory experiments (Hadziioannou et al., 2009; Zotz-Wilson et al., 2019) and to locate these (Snieder & Vrijlandt, 2005; Larose et al., 2010; Rossetto et al., 2011; Planès et al., 2015).

In a previous study by Zotz-Wilson et al. (2019), the use of coda wave interferometry with P-wave to monitor failure in UCS experiments has been shown. Barnhoorn et al. (2018), and Zhubayev et al. (2016) show that attenuation factor Q can be used to describe the start of fracture formation in UCS experiments. We extend both these studies to S-waves and tri-axial experiments to show both coda wave interferometry and attenuation can be used for forecasting the failure of rock samples in the laboratory.

2 Methods

2.1 Experimental Procedure

Shear wave propagation is influenced by changes in density and elastic moduli caused by structural changes due to deformation. We show different applications of acoustic measurements to monitor the structural changes within a Red Pfaelzer sandstone sample. These sandstones are used as an analog to Groningen reservoir rock and the properties of the individual sample are listed in Table 1. The eight rock samples have a porosity between 22% and 25% and fairly homogeneous composition. Used are cylindrical core samples with a diameter of 30 $\pm$ 0.5 mm and 60 $\pm$ 2 mm length, such that the length/diameter ratio is 1:2. A total of 8 uni-axially deformation experiments are performed at different confining pressures ranging from 25 to 400 bar and one UCS experiment (or 0 bar confining pressure). Simultaneously to the loading of the rock, acoustic transmission measurements are done. This combined setup enables us to measure the wave properties under changing stress conditions.

The experiments are performed with samples saturated with tap water at room temperature. First, the samples are brought up to the confining pressure in steps of 10 bar, such that the axial stress is always higher than the horizontal stress. After reaching the desired confining pressure, it is then set constant for the entire experiment. The samples are deformed at a constant strain rate of 0.005 s^{-1} and the shortening of the sample is recorded with two linear variable displacement transducers (LVDT's), and the stress using a load cell positioned above the sample (Figure 1).

The acoustic measurements are performed using two S-wave transducers, with a peak operating frequency of 1 MHz. The two axial transducers are integrated into the pistons in the loading system with a source at the top and receiver at the bottom, such that the polarization of the shear source and receiver transducers was always aligned. The acoustic signals are recorded every 10 seconds for 100 μs and are a stack of 256 (S-) waves to increase the signal-to-noise ratio. The acoustic monitoring started immedi-

Table 1. Summary of the Red Pfaelzer samples, confining pressure, porosity, length, diameter and Young's Modulus. All samples were water saturated.

Sample	P_c [bar]	ϕ [%]	L [mm]	D [mm]	E [GPa]
RF610	0	23.35	60.30	29.75	8.60
RF613	25	23.48	60.25	29.65	9.79
RF28	50	23.44	60.60	29.65	10.83
RF23	100	24.94	61.70	29.65	12.44
RF68	200	23.82	61.65	29.65	15.94
RF614	200	22.72	60.40	29.55	13.39
RF69	400	22.20	60.35	29.70	13.74
RF615	400	23.25	60.55	29.75	13.44

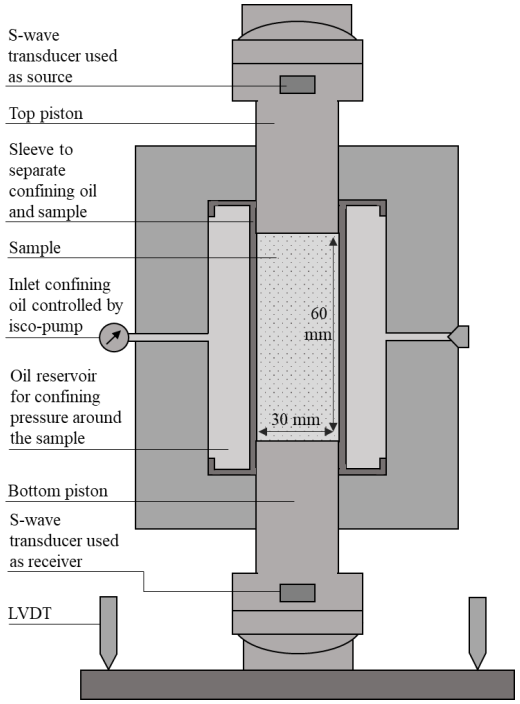

Figure 1. Schematic illustration of instrumented Hoek cell with S-wave transducers integrated into the pistons. The shortening of the sample was recorded with two linear variable displacement transducers (LVDT's), which record the total (vertical) movement of the loading plate.

ately after starting the deformation and continued during the whole duration of the deformation experiment.

2.2 Data Analysis

To monitor the onset and development of fracturing within the rock the coda wave, the attenuation, and transmissivity of the recorded waves are investigated. The coda wave is used to monitor the change in scattering properties, while the Q-factor, energy, and transmissivity are all a proxy of attenuation. The moment the scattering and attenuation effect of the formed fractures exceeds the effect of shortening and compaction is used as an indicator of fracture formation and upcoming failure. Coda Wave Interfer-

ometry is used to monitor velocity change between two recorded waves. Comparing the wavefields is done with a cross-correlation (CC), for a time window of width $2t_w$and centered around time t_k, and reached its maximum if the travel time perturbation δt across all possible perturbed paths P is $\delta t = t_s$. Assuming the time shift is constant in the considered time window, the velocity change (dv/v) can be written as $\delta v/v = \delta t/t$. Additional to the velocity change, the decorrelation coefficient is determined to investigate the changes in material scattering (Planès et al., 2014, 2015). The method of coda wave decorrelation introduced by Larose et al. (2010) is based on the theory of Snieder (2006). The decorrelation coefficient K, also described in Zotz-Wilson et al. (2019), is formulated as

$$K(t_s) = 1 - CC(t_s) = 1 - \frac{\int_{t_k-t_w}^{t_k+t_w} u_{p_j-N}(t) u_{p_j}(t+t_s)dt}{\sqrt{\int_{t_k-t_w}^{t_k+t_w} u^2_{p_j-N}(t)dt \int_{t_k-t_w}^{t_k+t_w} u^2_{p_j}(t)dt}}, \tag{1}$$

where N is the number of measurements the reference wavefield $u_(p_j - N)(t)$ is lagging behind the to be correlated wavefield $u_(p_j)(t)$ (Figure 2). While, the coda waves seem random due to the complex paths they take through the medium, the changes they are subjected to are strongly related to the position and strength of the changes in the medium (Planès et al., 2014). K is related to the changes in material scattering due to the addition of scatterers (Planès et al., 2014, 2015), such as the addition or removal of fractures. The scattering in a medium along the transport mean free path l can be described using the cross-sectional area of a single scatterer σ and the density of scatterers ρ (Planès et al., 2014). The total scattering coefficient as described by Aki and Chouet (1975) is given by $g_0 = \rho\sigma = l^{-1}$. Following the theory in Aki and Chouet (1975), we can rewrite the coda decorrelation in terms of the scattering coefficient (g_0) between a perturbed (p) and unperturbed (u) medium (Zotz-Wilson, 2020).

$$K(t) = \frac{v_0}{2} t |\Delta g_{0_{p-u}}|, \tag{2}$$

where $K(t)$ is the theoretical decorrelation coefficient, t the time in the coda and v_0 the velocity in the medium. Using a rolling reference, the changes in the absolute value of $|g_0|$ are monitored as a rate of change (Zotz-Wilson, 2020). In these deformation experiments, the change in scattering is mostly attributed to the closure or formation and growth of micro-fractures. The formation of micro-fractures, leading to failure, result in an increase in the total scattering cross-section σ and the number density of scatterers ρ, both contributing to an increase of the total scattering coefficient. Closure of pre-existing pore space (such as micro-fractures) and compaction of the medium cause a reduction in the scattering cross-sectional area and thus a reduction in K. During compaction and closure pre-existing pore space, the attenuation is expected to decrease and energy and transmissivity to increase.

While the formation and growth of micro-fractures increases the attenuation and causes causing the waves to lose energy and an increased arrival time. The ultrasonic attenuation is determined using the laboratory method by Toksoz et al. (1979) also described in Zhubayev et al. (2016); Barnhoorn et al. (2018). Assuming a constant Q, the spectral ratio is written as

$$\ln \frac{A_1}{A_2} = (\beta_2 - \beta_1) x f + \ln \frac{G_1}{G_2}, \tag{3}$$

where A_i is the Fourier amplitude, f is the frequency, x the propagation distance and G_i is a scaling factor for spherical spreading independent of frequency. i=1 refers

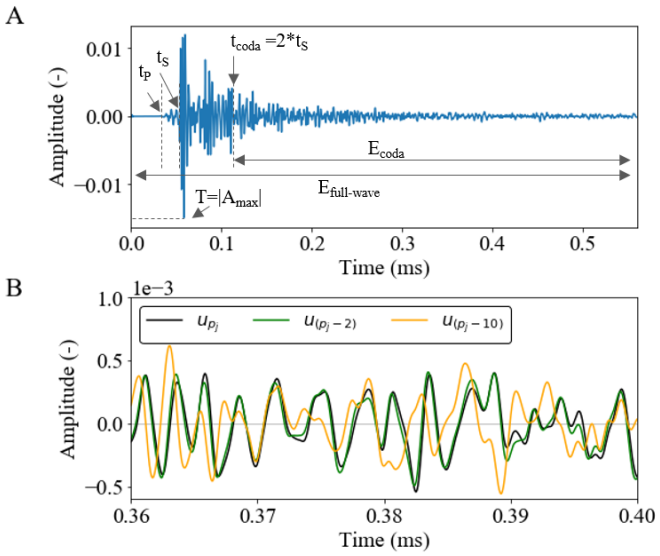

Figure 2. Showing recorded transmission wavelets. A showing the arrival times of P-wave (t_P), S-wave (t_S), and the start of the coda (t_{coda}). The range used for the energy calculation is indicated for the energy of the total- and coda wave as well as the maximum amplitude for the transmissivity. B showing a part of the coda of three wavelets. Where u_{p_j} is the to-be correlated wavefield and is lagging behind the reference wavefield by N=2 and N=10.

to the aluminium reference and 2 to the rock sample. β_i is related to the quality factor by

$$Q_i = \frac{\pi}{\beta_i V}, \tag{4}$$

where V is the P- or S- velocity and β_1 can be assumed to be zero, due to the very low attenuation of the aluminium. The energy of waves can be a good method for crack monitoring (Michaels et al., 2005; Mi et al., 2006) and is approximated as $E(\sigma) = \int_{t_2}^{t_1} u^2(t;\sigma)dt$, where $u(t;\sigma)$is the recorded waveform (Michaels et al., 2005; Mi et al., 2006; Sagar, 2009; Khazaei et al., 2015). The transmissivity is defined as $T = |A_{max}|$, which is the maximum amplitude of the recorded S-wave (Figure 2).

3 Results

The deformation of rock samples in the laboratory are commonly characterized in 5 stages: crack closure, the elastic stage, stable crack growth, and unstable cracking resulting in rock failure (Bieniawski, 1967; Eberhardt et al., 1999; Zhou et al., 2018). The stress-strain curves for the tested confining pressures (Figure 3) show a non-linear increase ate low stresses caused by the initial setting of the machine, elastic compaction of the rock, and closure of existing pore space (e.g. the closure of micro-cracks pre-existing in the sample (Walsh, 1965; Bieniawski, 1967; Eberhardt et al., 1999; Zhou et al., 2018). This is followed by an elastic (reversible) deformation stage, where a linear stiffening of the rock matrix is expected, visible as a linear gradient in the stress-strain curves. After the elastic stage, the stress-strain curve shows non-linear behaviour, indicating the start of inelastic (permanent) deformation, and describing the formation of the first micro-

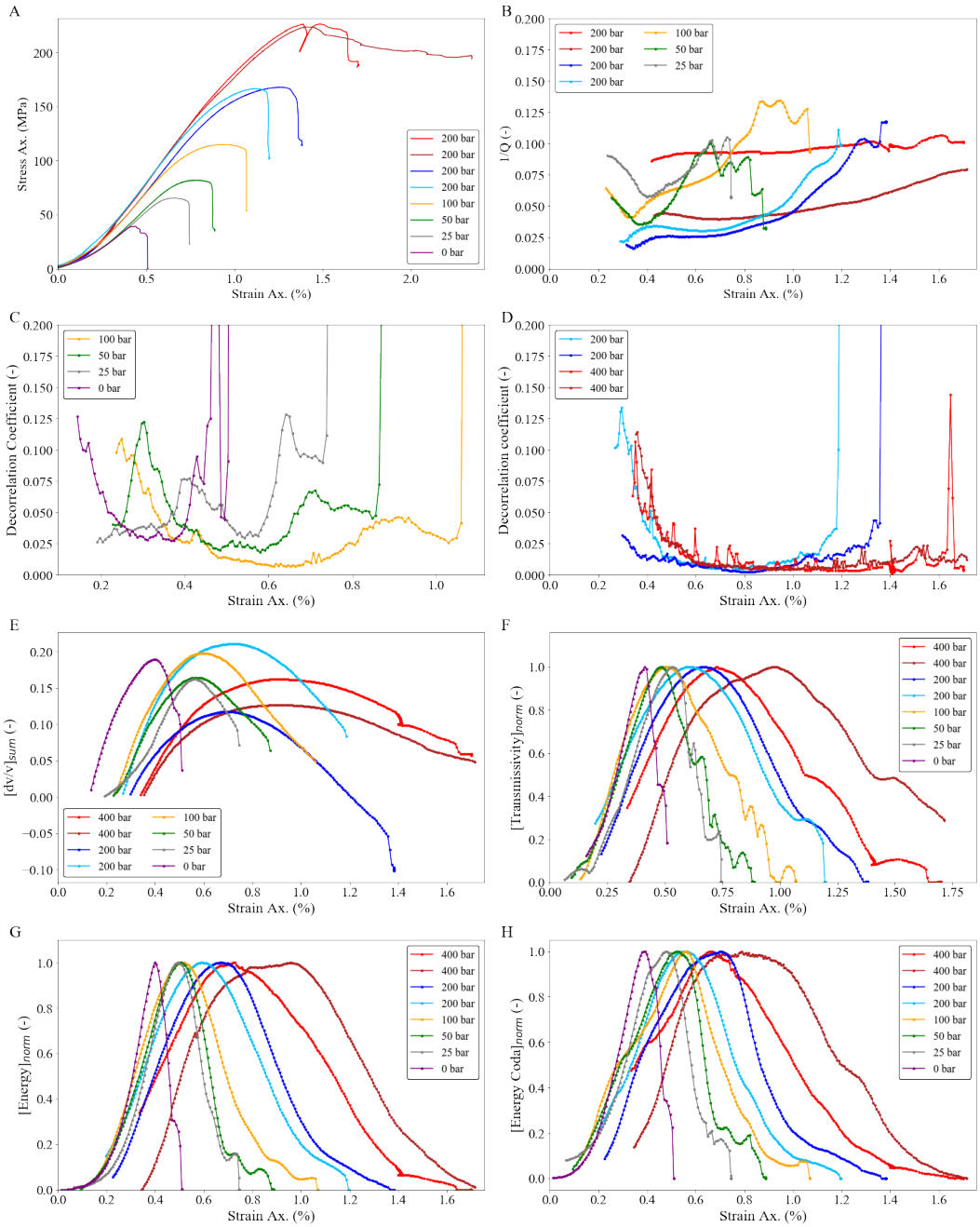

Figure 3. The acoustic parameters, and stress - strain during deformation experiment for all confining pressures. A showing the stress-strain relations. B showing the evolution of the attenuation 1/Q during deformation. C and D show the evolution of the decorrelation coefficient K for the lower and higher confining pressures. E shows the cumulative velocity change $[\mathrm{dv/v}]_{sum}$. F shows the evolution of the transmissivity T, normalized to the maximum of each experiment for better comparison. G and H show the energy of the full wave E_T and energy of the coda E_C, respectively. The values of each are normalized to their max for better comparison.

fractures (Barnhoorn et al., 2010). The crack formation continues until the stresses drop drastically, indicating the failure of the sample. Increasing the confining pressure leads to an increase of maximum strength and young's modulus of the sample.

Simultaneously to deformation, acoustic measurements were performed. CWD was used to monitor structural and velocity changes in the medium, following the results of Zotz-Wilson et al. (2019). K shows an average of 10 independent correlation windows, with the first starting at 2 times the S-arrival time ($t_{coda} = 2{*}t_S$) (Fehler et al., 1992; Pujades et al., 1997), in total the coda windows span 0.84ms. Using a rolling reference, the decorrelation coefficient K is a measure of change in the absolute value of $|g_0|$, therefore, a decreasing trend indicates a reduction in the scattering of the waveform compared to its previous. A reduction is visible at the start of the experiments for each tested confining pressure (Figure 3). This reduction is followed by a plateau of limited change in K, with thereafter an increase indicating an increasing scattering coefficient, during the deformation stage of formation and growth of (micro-) fractures.

Additionally to K, the velocity change during the experiment was determined using CWI. The CWI, using a rolling reference, gives the rate of change in velocity, by cumulative summation of the average relative velocity change, the velocity change during the experiment is obtained. This shows a hyperbolic trends indicating the compaction and formation and growth of (micro-) fractures during the experiments. The steeper hyperbola's for lower confined pressures show a more rapid deformation compared to higher confining pressures, where more pressure, thus more time is needed to achieve rock failure. Similar hyperbolic trends can be seen in the energy and transmissivity data, where the initial increase can be explained by the compaction of the rock matrix and the following decrease by the formation of micro-fractures (Shah & Hirose, 2010; Zotz-Wilson et al., 2019; Zotz-Wilson, 2020). Additionally to the energy and transmissivity, the evolution of the ultrasonic attenuation and frequency content of the waveforms provide insight into the deformation of the sandstones.

The energy of waves can be absorbed in large amounts by fractures. Changes in acoustic waveforms are detected when the attenuation effects due to fracture formation are larger than the compaction and shortening effect due to loading. During loading, the samples are subjected to a constant strain rate. This results in shortening and compaction and causes a shorter direct travel path, as well as a faster path, due to increased velocity, for the transmitted acoustic waves. Together with the closure of pre-existing porespace in the rock matrix these result in an increase in energy, transmissivity, and relative velocity (Figure 3). The fractures induced by this continued deformation reverse this effect, decreasing the velocity of the matrix and increasing attenuation causing the waves to lose energy and arrive at an increased arrival time. The competition between these factors results in the hyperbolic trends of transmissivity, velocity change and energy. The peak of these hyperbola's, the change from an increasing to decreasing trend, is around the point the gradient of the stress strain curve changes to non-linearity and shows the first indication of permanent deformation, thus (micro-) fracture formation and growth. Within these hyperbolic trends, a more complex pattern in the S-wave amplitudes emerges around the peak stress, for the lower confining pressures. This pattern is also visible in the evolution of the Q-factor (attenuation), which is inversely related to the energy and transmissivity of the S-waves. The frequency content of the recorded wave changed during the experiment. The normalized amplitude spectra of the frequency show a shift towards the lower frequencies, due to the increased presence of micro-fractures until after failure the high frequencies are mostly attenuated and the lower persevere.

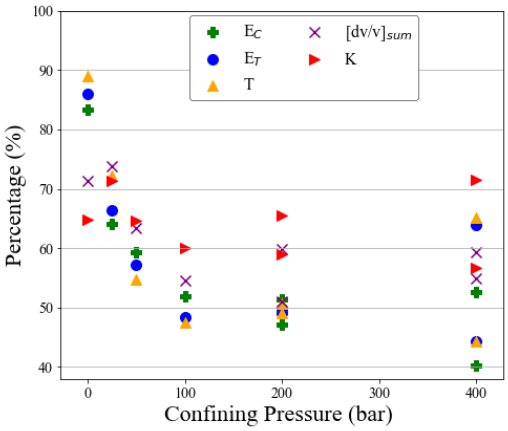

Figure 4. Appearance of the peak in the energy of the full wave E_T and coda wave E_C, the cumulative velocity change $[dv/v]_{sum}$, and the transmissivity T, as well as the minimum of the decorrelation coefficient K as precursor relative to the failure of the sample.

4 Discussion

4.1 Acoustic Monitoring and forecasting failure

The first sign of permanent deformation, namely the formation of (micro-) fractures resulting in failure of the sample, is the change to non-linearity in the gradient of the stress-strain relation. However, this stress-strain relation is impossible to determine in-situ (i.e. landslides, earthquakes, etc.). To detect deformation without stress and/or strain measurements, we focused on the change in acoustic response throughout deformation, using the advantage that active source methods do not rely on acoustic emission to detect any deformation, and thus can be used to monitor both aseismic and seismic deformation. The attenuation and scattering properties of the waves change due to the formation and growth of the (micro-) fractures in the samples. To monitor the change in scattering and relative velocity change dv/v, coda wave interferometry is used, while the Q-factor, energy E, and transmissivity T are all a proxy of attenuation. We show that while none of these methods are preferable in detecting the formation of (micro-) cracks, combining them gives a better insight into the failing rock samples.

Precursors to failure were determined from the waveform attributes. The evolution of the energy, relative velocity change, and transmissivity show a clear change in slope as the fractures formed are detected. The decorrelation coefficient K shows an increase in scattering when the fractures are formed and detected by the coda. Therefore, the minimum before this increasing trend in the K, and the peaks of E, dv/v, and T are used as the earliest precursor to the imminent failure of the sample. The occurrence of these precursors is plotted relative to failure, where at 100% failure occurs (Figure 4). For UCS experiments precursors obtained from CWD are significantly earlier than the precursors based on attenuation properties, 65% to 72%, and 84% to 88% respectively. This changes with increasing pressure, where the precursors based on attenuation are generally earlier. Although, especially at higher pressures K has an extended period of minimal change, giving a more detailed understanding of the process of deformation. Which of the precursors to failure is the first varies and comes as early as 40% of failure for 400 bar confining pressure. At higher pressures, the precursors are relatively earlier, but also show a bigger spread. This shows that when combining the different precursory signals, a more robust warning system for failure can be obtained, which on average forecasts at stress-strain conditions before 70% of failure.

To forecast the upcoming failure of the sample, we deployed a traffic light warning system (TLS) based on the interpretation of the processed acoustic data. From the stress-strain data is known that at the start of the experiment the rock matrix stiffens, therefore strengthening. Afterward, the first fractures start to form which ultimately leads to failure of the samples. We split the data into three zones, according to the traffic light, using solely the precursors obtained from the acoustic data (Figure 5).

1. The first stage of the traffic light is the green zone. In this stage K decreases, indicating the closure of pre-existing pore-space, stiffening, and compaction of the rock. During this stage E, dv/v, and T increase, indicating a reduction in attenuation, and compaction of the sample. The Q-factor, showing the ultrasonic attenuation, shows a slight reduction and increase in this zone indicating the attenuation is more or less constant. Finally, the frequency shows an increase in high-frequency content. Due to the closure of pre-existing pore-space and compaction, the high frequencies are less attenuated. Therefore, when K decreases, but the E, A, and dv/v increases, and the frequency content remains similar or shift a bit to the higher frequencies, the rock is far from failure, even strengthens. According to our traffic light, it is green or safe.
2. The next step in the traffic light is orange. During this stage E, dv/v, and T change to a decreasing trend indicating the attenuation effect due to newly formed (micro-) fractures is stronger than the continued compaction and shortening of the sample. However, K does not increase indicating that no major increase in scattering is measured. This orange stage can therefore be classified as a stage of higher alert in which failure is expected, but not yet imminent.
3. The last step of the traffic light is red, this stage represents the warning failure is imminent. The warning stage starts when K shows an increase in scattering, giving a clear indication (micro-) fractures are formed. A clear indication of fracture formation and thus upcoming failure is present when the energies, transmissivity, and the relative velocity change show a decreasing trend and the decorrelation coefficient starts to increase. Additionally, the frequency content of the recorded wave shifts towards the lower frequencies as the higher frequencies are attenuated more, due to increased formation and growth of (micro-) fractures.

Experiment to experiment, the first precursor varies (Figure 4), but for forecasting purposes, not one precursory signal is superior over the other. By combining the various analyses techniques, the impact of the sensitivity of a single parameter is limited and a more robust TLS prediction can be made, without having to do multiple measurements. Even though precursory signals vary for confining pressure, the results show that the trend in the processed data of the S-waves is very similar for all tested confining pressures. Therefore, these techniques can be deployed for monitoring the failure of rocks, at any depth or pressure condition, before any passive system would detect any seismicity. Monitoring is possible at any arbitrary point in time or stress condition, using a rolling reference and by using the traffic light system, the frequency of measurements can be increased near failure to obtain an even more accurate forecast. An additional advantage of monitoring is that only the final values are necessary to be saved, as mostly the trend is leading in the forecasting or traffic light system. A fast monitoring system could be deployed where T, E, and K are calculated, saved, and added to previously measured values and the full waveform discarded when data storage and/or budget is limited. We note that at lower tested confining pressure after the peak strength, thus failure point was reached, the K shows a small decrease in value. The decorrelation is still much higher than during the elastic stage of deformation before. It does show deformation processes are occurring, but the difference between succeeding waves decreases. This shows the importance of combining various analyses techniques. Limiting the dependence on K, which shows detail in the changing scattering properties during the deformation, creates a more robust prediction.

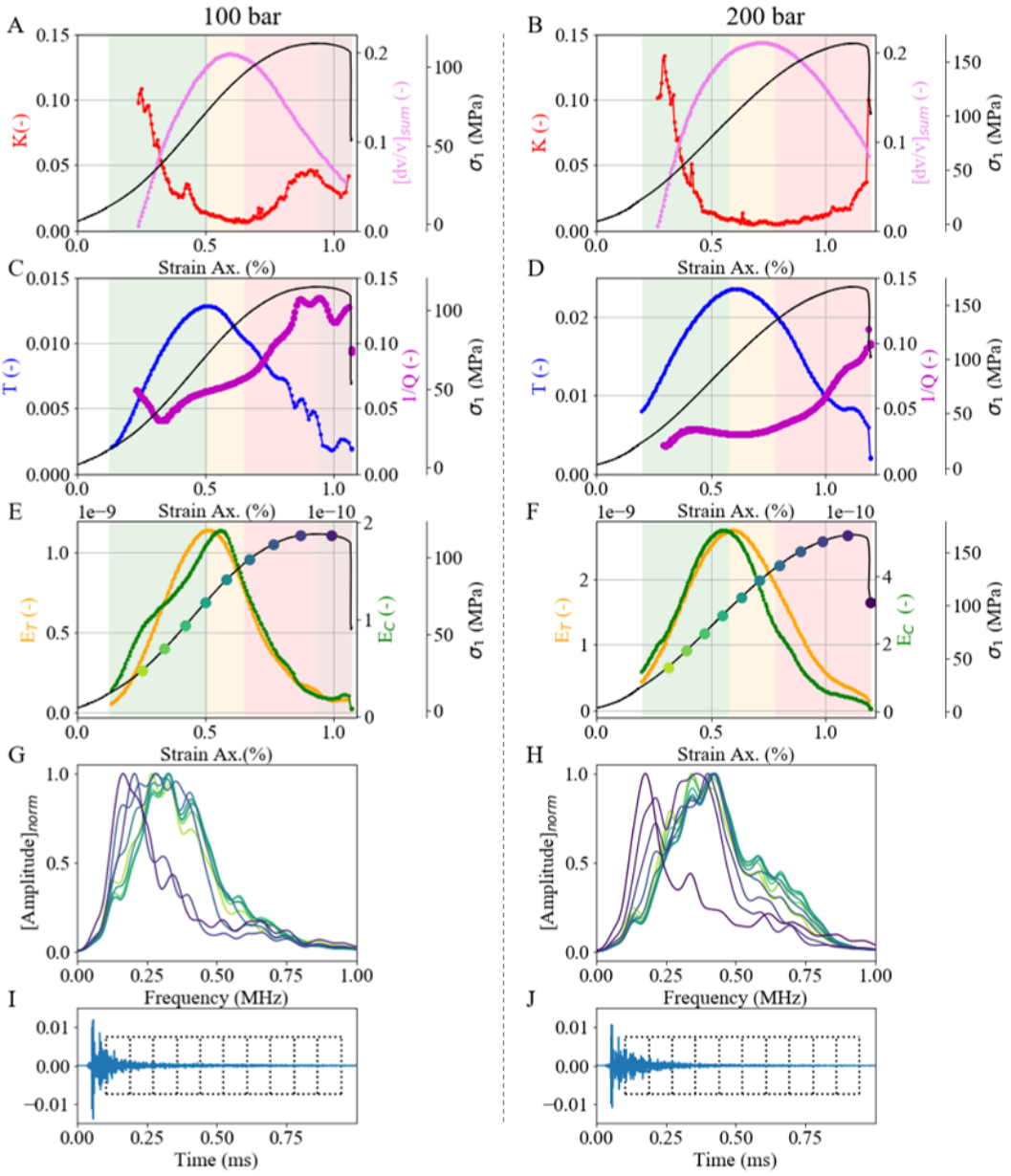

Figure 5. Active acoustic precursory signals during the deformation at 100 and 200 bar confining pressure. Showing the cumulative velocity change from CWI dv/v_{sum} and decorrelation coefficient K in A, B, the attenuation 1/Q and transmissivity T in C, D, and the energy of the full wave E_T and coda wave E_C in E, F together with the stress-strain relation. G, H showing the changing frequency content of the recorded waves during deformation. E and F show the stage of deformation of the frequency content plotted, in corresponding colour. I and J show a recorded waveform during deformation, the 10 decorrelation windows are visualized, with the first starting at 2 times the S-arrival time ($t_{coda} = 2 * t_S$), and a total length of 0.84ms. The coloured zones in A-F show the three stages of the traffic light warning system (TLS).

The timeline for rock failure in the laboratory can be very different from failure in the field, whereas failure in the laboratory is achieved in under an hour, in the field achieving failure can take years. The precursors we showed in this paper, can be used to forecast approximately 70% from failure. Whereas in a laboratory setting this might be seconds or minutes. This could be hours or days at field scale which can provide time for mitigation measures. The application and scalability of active acoustic monitoring from laboratory to field scale will have to be researched. However, research shows precursory signals were measured at a field scale. Niu et al. (2008), showed stress-induced changes in crack properties during co-seismic slip using active source cross-well experiment at the San Andreas Fault or Chiarabba et al. (2020), who showed a local P-wave velocity reduction near the hypocentre for a few weeks before the mainshock using seismic tomography at the fault zone which participated in the 2016 M6.5 Norcia earthquake, Italy.

4.2 Effect of pressure

The competition between the attenuation and scattering effect of fracture formation and compaction and shortening of the sample results in a clear precursory signal for all tested confining pressures. The difference between pressures tested, for our purpose of forecasting failure are of lesser importance, but give us some more insight into the process of deformation and sensitivity of the used S-waves in the detection of microfractures. The deformation experiments were performed at various confining pressures to investigate a possible effect of pressure on the acoustic response for monitoring. Pressure affects the fracturing process, at high confining pressures shear fractures rather than tensile fractures form. These shear fractures will be created with small apertures or are closed due to the high confining pressures. Differences due to pressure are visible in the acoustic response.

4.2.1 Deformation Rate

The deformation experiments are all performed with a loading rate of 0.005s^{-1}, however, at high confining pressure, larger stresses are needed to achieve failure of the sample. Therefore, the deformation rate is relatively slower for high confined experiments. These rock samples have a lengthier elastic stage and a slower fracture formation with small or closed apertures causing less additional scattering than rapid fracture formation. During this transition from elastic to inelastic behaviour, the K shows a platform, indicating little change. Due to the (relative) slower deformation at high pressure, relatively more acoustic data points are recorded per deformation stage. Consequently, less change in the scattering in the medium from waveform to reference waveform is detected. This results in a more distinct platform in K, which is increasingly more pronounced for higher confining pressures. Once more fractures start to form and the rock sample starts to fail, the increasing scattering in the medium causes the trend in the decorrelation coefficient to rapidly increase towards the failure of the sample.

This also implies that, at higher confining pressures, the deformation is better monitored than at low confining pressures, as a constant sampling rate of 10 sec was used. Therefore, the deformation at 400 bar confining pressure was sampled best. During the deformation, K shows several sharp peaks showing rapid, but short changes in the sample (Figure 3). From the nature of the rolling reference, these peaks can be interpreted as the change from the signal before. Crack formation increases the amount of scattering, thus K. If at the sampling time no new crack is formed, no additional scattering is created, thus K goes down again. We interpret these peaks at the start of the experiment as the sharp closure of larger or a couple of pre-existing fractures present in the rock sample. While during a later stage of deformation these peaks indicate the formation of micro-cracks, large enough to be sampled by the acoustic waves and frequency used. When deformation is fast, crack formation follows each other in quick succession, resulting in an increase in scattering and K, without individual crack formation visible.

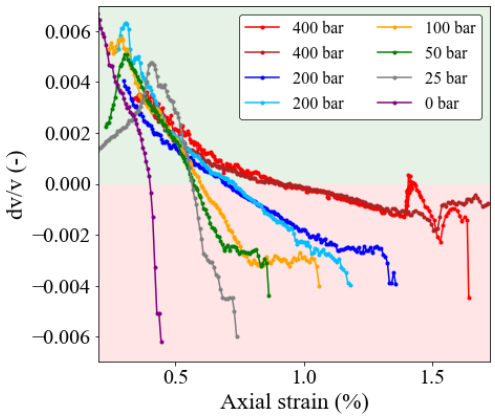

Figure 6. The rate of velocity change dv/v during deformation for each confining pressure tested. Showing the relative deformation rate changes with pressure for a constant loading rate of $0.0005 s^{-1}$

This implies that for slow deformation and a high sampling rate, the separate crack formation can be monitored (if the waves are sensitive enough).

This relative loading rate effect and deformation speed are also visible in the velocity change during deformation, when plotted cumulative to represent the absolute velocity change the graphs differs from pressure to pressure, however when we plot the derivative, the rate of the velocity change decreases with confining pressure, showing a slower rate of deformation at higher pressure (Figure 6).

4.2.2 Deformation around peak strength

The difference in deformation due to pressure is also visible in the maxima of the waveform attributes (Figure 7). Differences due to pressure are visible in the acoustic response, as the attenuation effect and scattering properties differ between open tensile, and small aperture or closed shear fractures. The maximum value of K obtained during the failure of the sample shows a decreasing trend with increasing pressure. Opposite, the maximum energy and transmissivity measured increase with confining pressure. The source wavelet for all experiments remained constant, due to increased compaction more of the initial wave energy is preserved at higher initial confining stresses. A reduced scattering effect of the shear compared to tensile fractures results in decreasing values of K. Implicating that tensile fractures or fractures with a bigger aperture are better detected. Due to the higher scattering nature of the tensile fracture.

Near the failure point of the stressed rock samples, the formed micro-fractures start to connect and form larger-scale shear fractures. At lower confining pressures, a more complex pattern in the transmissivity emerges around the peak stress (Figure 3). The attenuation (Q-factor), energy, and transmissivity for the lower confining pressures oscillate. We suggest this oscillating behaviour observed in our data, is the detection of the connecting shear fractures near failure. The transmissivity and energy increase due to the continued shortening and compaction of the sample. The moment the fractures are formed and connected into larger ones, the attenuation increases, and the energies and transmissivity drop. While the sample is not failing yet and is still shortened and compacted, the formed fractures (partially) close and the attenuation decreases until the next local failure forms the next larger fracture, resulting in the observed oscillations. This oscillation is only visible when the sample show less brittle behaviour, when the sam-

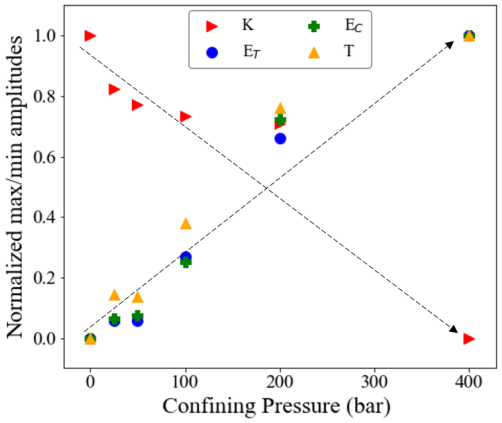

Figure 7. The maximum value recorded for each precursor. Showing decreasing trend with pressure in decorrelation coefficient K, and an increasing trend in energy of the full wave E_T and coda wave E_C, and transmissivity T.

ple collapses at or very close to peak strength this oscillation is not observed suggesting all the micro-fractures connect rapidly in one large shear fracture. At higher confining pressure the potential to form fractures with aperture is very small, therefore we state that this oscillation is not present due to the lack of sensitivity of the acoustic waves and less brittle behaviour of the samples at higher pressures.

A similar effect is visible in K and dv/v for the lower tested confining pressures around the peak strength of the rock. At lower pressure K peaks around the peak stress of the sample. This intermediate peak is largest at low confining pressure and decreases in strength until not present towards higher pressures. The velocity shows a linear decrease during this period of deformation, opposed to an accelerating decrease, both indicating the rapid increase of fractures (increase in scattering) formation has stopped. Also, the frequency content is already shifted after peak strength to a lower frequency range, indicating most fractures attenuating the higher frequencies were already formed.

5 Conclusion

Ultrasonic experiments have been conducted on Red Pfaelzer sandstones (analog to the Groningen reservoir rock) to investigate the potential of active acoustic measurements in forecasting the upcoming failure. Active acoustic monitoring can monitor the changes in the subsurface, while passive methods could be late in detecting the upcoming failure. Our results show the failure of the tested samples can be forecasted from 40 to 70% of the failure point. A robust prediction can be made by combining the various analyses techniques, without having to do multiple measurements. Which precursor to failure first varies, and comes as early as 40% of failure at high pressure, but for forecasting purposes, not one precursory signal is superior over the other.

In this study, the stress-strain relations were available, therefore the small details in the acoustic response could be explained by relating the signals to the deformation stages of the stress-strain relation. The precursors show small differences between tested confining pressures, but as the trends are very similar, we argue that the proposed traffic light forecasting system is applicable for forecasting failure at various depths and or stress conditions. monitoring can be started at any arbitrary point in time or stress condition using a rolling reference, and as mostly the trend is leading in the forecasting or

traffic light system, only the final values are necessary to be saved, which can potentially saves costs. For field measurements, additional research and feasibility studies will have to be performed, but the shown monitoring methods in this paper are applicable in field situations when stress-strain measurements are not possible. Contributing to a robust monitoring technique that can detect small stress-induced changes in the subsurface and use these for a better prediction and thus mitigation of failure (and seismicity) in the subsurface.

Acknowledgments

This research was (partially) funded by NWO Science domain (NWO-ENW), project DEEP.NL.2018.048. All the data in this paper will be made available on the 4TU data repository: *https://data.4tu.nl/info/en/*.

References

Aki, K., & Chouet, B. (1975). Origin of coda waves: Source, attenuation, and scattering effects. *Journal of Geophysical Research*, *80*(23), 3322–3342. doi: 10.1029/jb080i023p03322

Barnhoorn, A., Cox, S. F., Robinson, D. J., & Senden, T. (2010, sep). Stress- and fluid-driven failure during fracture array growth: Implications for coupled deformation and fluid flow in the crust. *Geology*, *38*(9), 779–782. doi: 10.1130/G31010.1

Barnhoorn, A., Verheij, J., Frehner, M., Zhubayev, A., & Houben, M. (2018). Experimental identification of the transition from elasticity to inelasticity from ultrasonic attenuation analyses. *Geophysics*, *83*(4), MR221–MR229. doi: 10.1190/geo2017-0534.1

Bieniawski, Z. T. (1967). Mechanism of brittle fracture of rock. Part I-theory of the fracture process. *International Journal of Rock Mechanics and Mining Sciences and*, *4*(4). doi: 10.1016/0148-9062(67)90030-7

Chiarabba, C., De Gori, P., Segou, M., & Cattaneo, M. (2020). Seismic velocity precursors to the 2016 Mw 6.5 Norcia (Italy) earthquake. *Geology*, *48*(9), 924–928. doi: 10.1130/G47048.1

Deroo, F., Kim, J.-Y., Qu, J., Sabra, K., & Jacobs, L. J. (2010). Detection of damage in concrete using diffuse ultrasound. *The Journal of the Acoustical Society of America*, *127*(6), 3315–3318. doi: 10.1121/1.3409480

Eberhardt, E., Stead, D., & Stimpson, B. (1999). Quantifying progressive pre-peak brittle fracture damage in rock during uniaxial compression. *International Journal of Rock Mechanics and Mining Sciences*, *36*(3), 361–380. doi: 10.1016/S0148-9062(99)00019-4

Fehler, M., Hoshiba, M., Sato, H., & Obara, K. (1992). Separation of scattering and intrinsic attenuation for the Kanto-Tokai region, Japan, using measurements of S-wave energy versus hypocentral distance. *Geophysical Journal International*, *108*(3), 787–800. doi: 10.1111/j.1365-246X.1992.tb03470.x

Grêt, A., Snieder, R., Aster, R. C., & Kyle, P. R. (2005). Monitoring rapid temporal change in a volcano with coda wave interferometry. *Geophysical Research Letters*, *32*(6), 1–4. doi: 10.1029/2004GL021143

Grêt, A., Snieder, R., & Özbay, U. (2006). Monitoring in situ stress changes in a mining environment with coda wave interferometry. *Geophysical Journal International*, *167*(2), 504–508. doi: 10.1111/j.1365-246X.2006.03097.x

Grêt, A., Snieder, R., & Scales, J. (2006). Time-lapse monitoring of rock properties with coda wave interferometry. *Journal of Geophysical Research: Solid Earth*, *111*(3), 1–11. doi: 10.1029/2004JB003354

Hadziioannou, C., Larose, E., Coutant, O., Roux, P., & Campillo, M. (2009). Stability of monitoring weak changes in multiply scattering media with ambient

noise correlation: Laboratory experiments. *The Journal of the Acoustical Society of America*, *125*(6), 3688–3695. doi: 10.1121/1.3125345

Hall, S. A. (2009). *When geophysics met geomechanics: Imaging of geomechanical properties and processes using elastic waves* (VIII ed.; D. Kolymbas & G. Viggiani, Eds.). Springer. doi: 10.1007/978-3-642-03578-4

Khazaei, C., Hazzard, J., & Chalaturnyk, R. (2015). Damage quantification of intact rocks using acoustic emission energies recorded during uniaxial compression test and discrete element modeling. *Computers and Geotechnics*, *67*, 94–102. doi: 10.1016/j.compgeo.2015.02.012

Larose, E., Planes, T., Rossetto, V., & Margerin, L. (2010). Locating a small change in a multiple scattering environment. *Applied Physics Letters*, *96*(20), 1–4. doi: 10.1063/1.3431269

Mi, B., Michaels, J. E., & Michaels, T. E. (2006). An ultrasonic method for dynamic monitoring of fatigue crack initiation and growth. *The Journal of the Acoustical Society of America*, *119*(1), 74–85. doi: 10.1121/1.2139647

Michaels, J. E., Michaels, T. E., Mi, B., Cobb, A. C., & Stobbe, D. M. (2005). Self-calibrating ultrasonic methods for in-situ monitoring of fatigue crack progression. *AIP Conference Proceedings*, *760*(2005), 1765–1772. doi: 10.1063/1.1916884

Niederleithinger, E., Wang, X., Herbrand, M., & Müller, M. (2018). Processing ultrasonic data by coda wave interferometry to monitor load tests of concrete beams. *Sensors (Switzerland)*, *18*(6). doi: 10.3390/s18061971

Niu, F., Silver, P. G., Daley, T. M., Cheng, X., & Majer, E. L. (2008). Preseismic velocity changes observed from active source monitoring at the Parkfield SAFOD drill site. *Nature*, *454*(7201), 204–208. doi: 10.1038/nature07111

Niu, F., Silver, P. G., Nadeau, R. M., & McEvilly, T. V. (2003). Migration of seismic scatterers associated with the 1993 Parkfield aseismic transient event. *Nature*, *426*(6966), 544–548. doi: 10.1038/nature02151

Nur, A. (1971). Effects of stress on velocity anisotropy in rocks with cracks. *J Geophys Res*, *76*(8), 2022–2034. doi: 10.1029/jb076i008p02022

Planès, T., Larose, E., Margerin, L., Rossetto, V., & Sens-Schönfelder, C. (2014). Decorrelation and phase-shift of coda waves induced by local changes: Multiple scattering approach and numerical validation. *Waves in Random and Complex Media*, *24*(2), 99–125. doi: 10.1080/17455030.2014.880821

Planès, T., Larose, E., Rossetto, V., & Margerin, L. (2015). Imaging multiple local changes in heterogeneous media with diffuse waves. *The Journal of the Acoustical Society of America*, *137*(2), 660–667. doi: 10.1121/1.4906824

Poupinet, G., Ellsworth, W. L., & Frechet, J. (1984). Monitoring velocity variations in the crust using earthquake doublets: an application to the Calaveras fault, California (USA). *Journal of Geophysical Research*, *89*(B7), 5719–5731. doi: 10.1029/JB089iB07p05719

Pujades, L., Ugalde, A., Canas, J. A., Navarro, M., Badal, F. J., & Corchete, V. (1997). Intrinsic and scattering attenuation from observed seismic codas in the Almeria Basin (southeastern Iberian Peninsula). *Geophysical Journal International*, *129*, 281–291. doi: 10.1016/j.pepi.2004.02.004

Rossetto, V., Margerin, L., Planès, T., & Larose, É. (2011). Locating a weak change using diffuse waves: Theoretical approach and inversion procedure. *Journal of Applied Physics*, *109*(3). doi: 10.1063/1.3544503

Sagar, R. V. (2009). An experimental Study on Acoustic Emission Energy and Fracture Energy of Concrete. *Proceedings of the National Seminar & Exhibition on Non-Destructive Evaluation*, 225–228.

Schubnel, A., Benson, P. M., Thompson, B. D., Hazzard, J. F., & Paul Young, R. (2006). Quantifying Damage , Saturation and Anisotropy in Cracked Rocks by Inverting Elastic Wave Velocities. *Pure and Applied Geophysics*, *163*, 947–973. doi: 10.1007/s00024-006-0061-y

Shah, A. A., & Hirose, S. (2010). Nonlinear Ultrasonic Investigation of Concrete Damaged under Uniaxial Compression Step Loading. *Journal of Materials in Civil Engineering*, *22*(5), 476–484. doi: 10.1061/(asce)mt.1943-5533.0000050

Snieder, R. (2006). The theory of coda wave interferometry. *Pure and Applied Geophysics*, *163*(2-3), 455–473. doi: 10.1007/s00024-005-0026-6

Snieder, R., Grêt, A., Douma, H., & Scales, J. (2002). Coda wave interferometry for estimating nonlinear behavior in seismic velocity. *Science*, *295*(5563), 2253–2255. doi: 10.1126/science.1070015

Snieder, R., Prejean, S. G., & Johnson, J. B. (2006). Spatial variation in Mount St. Helens clones from coda wave analysis. *Centre for Wave Phenomena Consortium Project 2006*, 247–252.

Snieder, R., & Vrijlandt, M. (2005). Constraining the source separation with coda wave interferometry: Theory and application to earthquake doublets in the Hayward fault, California. *Journal of Geophysical Research: Solid Earth*, *110*(4), 1–15. doi: 10.1029/2004JB003317

Toksoz, M. N., Johnston, D. H., & Timur, A. (1979). Attenuation of Seismic Waves in Dry and Saturated Rocks -I. Laboratory measurements. *Geophysics*, *44*(4), 681–690. doi: 10.1190/1.1440970

Walsh, J. B. (1965, jan). The effect of cracks on the compressibility of rock. *Journal of Geophysical Research*, *70*(2), 381–389. doi: 10.1029/JZ070i002p00381

Xie, F., Ren, Y., Zhou, Y., Larose, E., & Baillet, L. (2018). Monitoring Local Changes in Granite Rock Under Biaxial Test: A Spatiotemporal Imaging Application With Diffuse Waves. *Journal of Geophysical Research: Solid Earth*, *123*(3), 2214–2227. doi: 10.1002/2017JB014940

Zhou, S., Xia, C., & Zhou, Y. (2018). A theoretical approach to quantify the effect of random cracks on rock deformation in uniaxial compression. *Journal of Geophysics and Engineering*, *15*(3), 627–637. doi: 10.1088/1742-2140/aaa1ad

Zhubayev, A., Houben, M. E., Smeulders, D. M., & Barnhoorn, A. (2016). Ultrasonic velocity and attenuation anisotropy of shales, Whitby, United Kingdom. *Geophysics*, *81*(1), D45–D56. doi: 10.1190/GEO2015-0211.1

Zotz-Wilson, R. (2020). *Coda-wave monitoring of continuously evolving material properties* (PhD dissertation, Delft University of Technology). doi: https://doi.org/10.4233/uuid:9c0b2f03-040b-4ec8-b669-951c5acf1f3b

Zotz-Wilson, R., Boerrigter, T., & Barnhoorn, A. (2019). Coda-wave monitoring of continuously evolving material properties and the precursory detection of yielding. *The Journal of the Acoustical Society of America*, *145*(2), 1060–1068. doi: 10.1121/1.5091012

Figure 1.

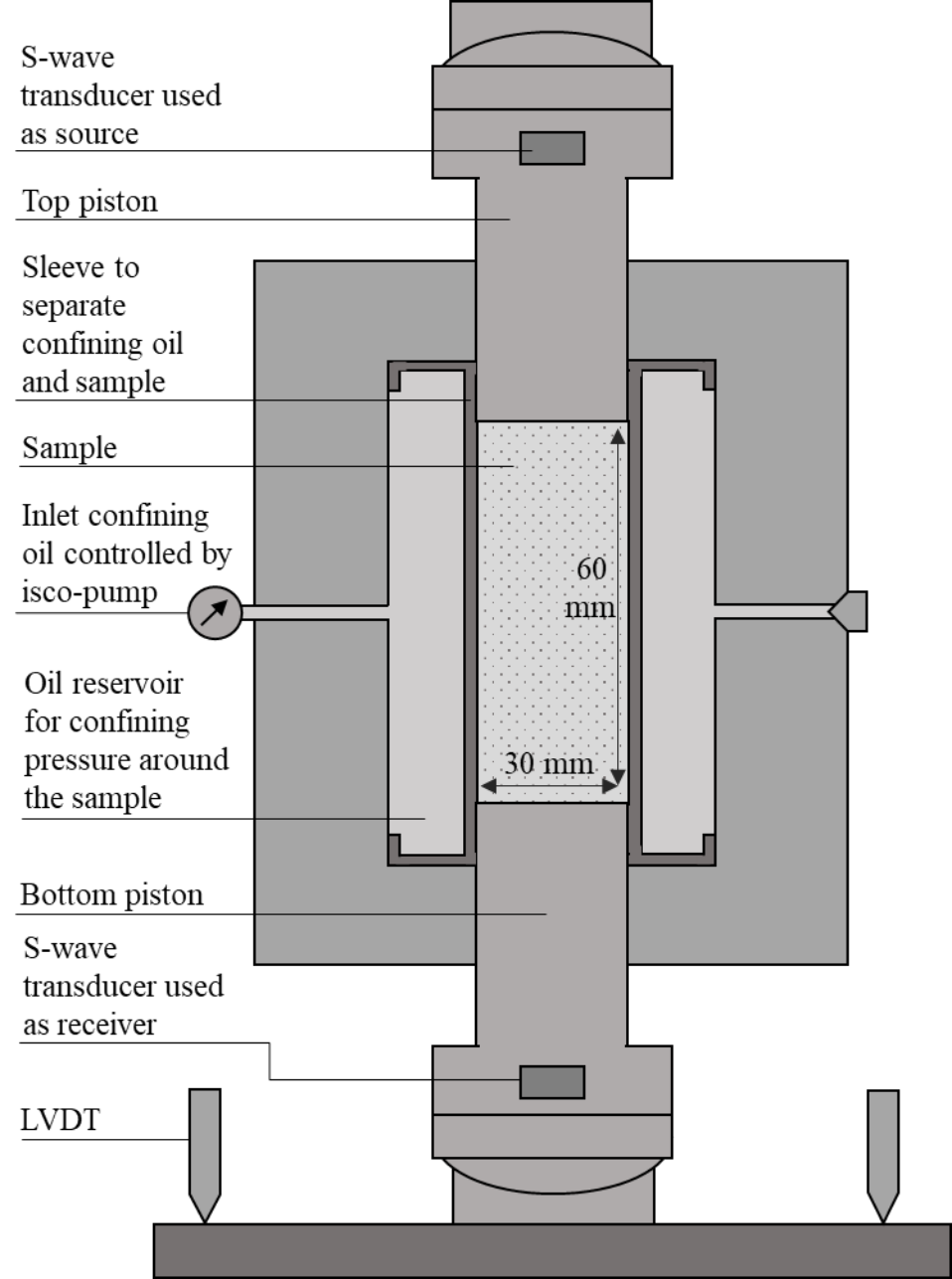
S-wave transducer used as source
Top piston
Sleeve to separate confining oil and sample
Sample
Inlet confining oil controlled by isco-pump
Oil reservoir for confining pressure around the sample
Bottom piston
S-wave transducer used as receiver
LVDT
60 mm
30 mm

Figure 2.

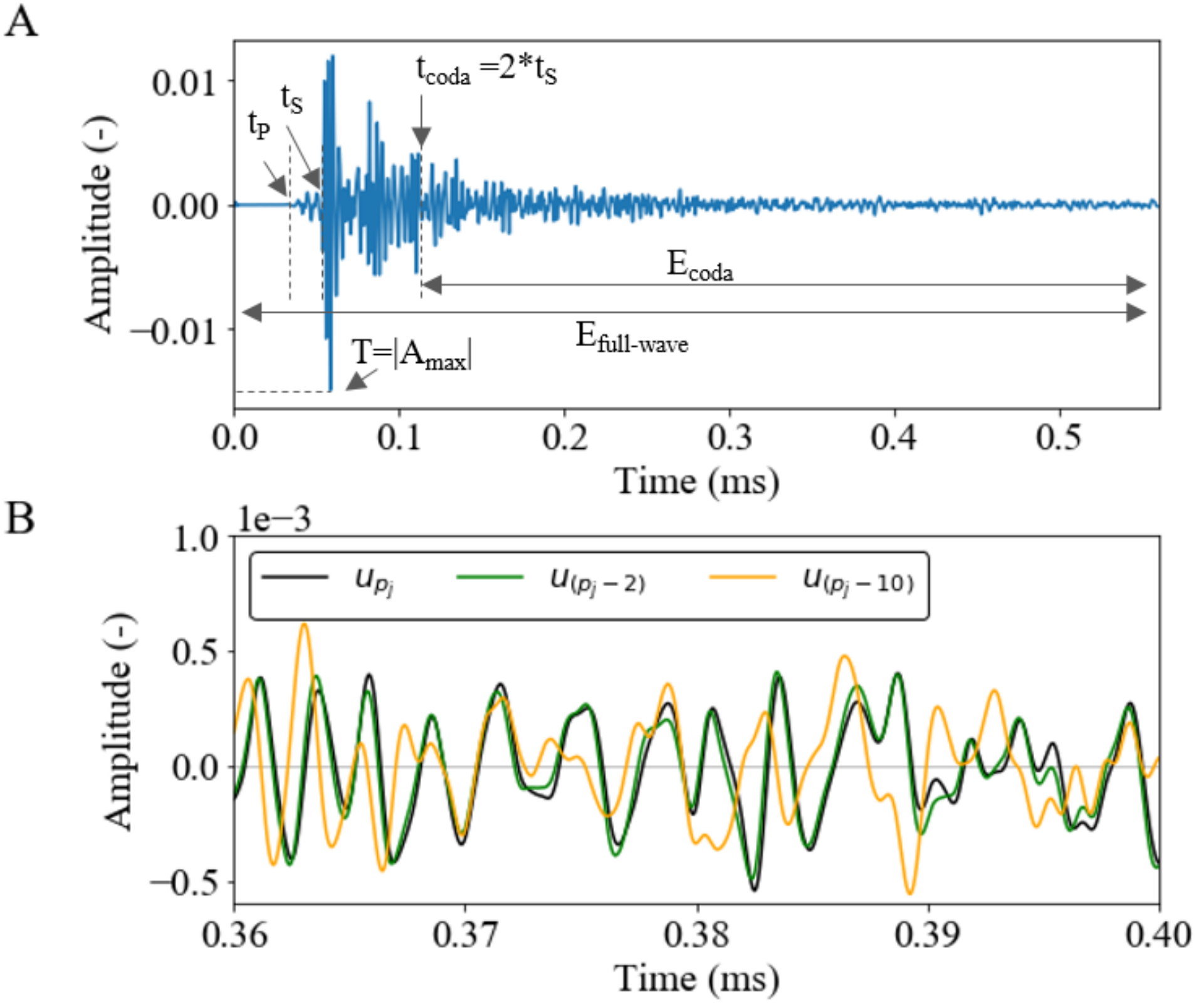
A
0.01
0.00
−0.01
Amplitude (-)
t_P
t_S
$t_{coda} = 2*t_S$
E_{coda}
$E_{full\text{-}wave}$
$T=|A_{max}|$
0.0
0.1
0.2
0.3
0.4
0.5
Time (ms)
B
1e−3
1.0
0.5
0.0
−0.5
Amplitude (-)
u_{p_j}
$u_{(p_j-2)}$
$u_{(p_j-10)}$
0.36
0.37
0.38
0.39
0.40
Time (ms)

Figure 3.

A

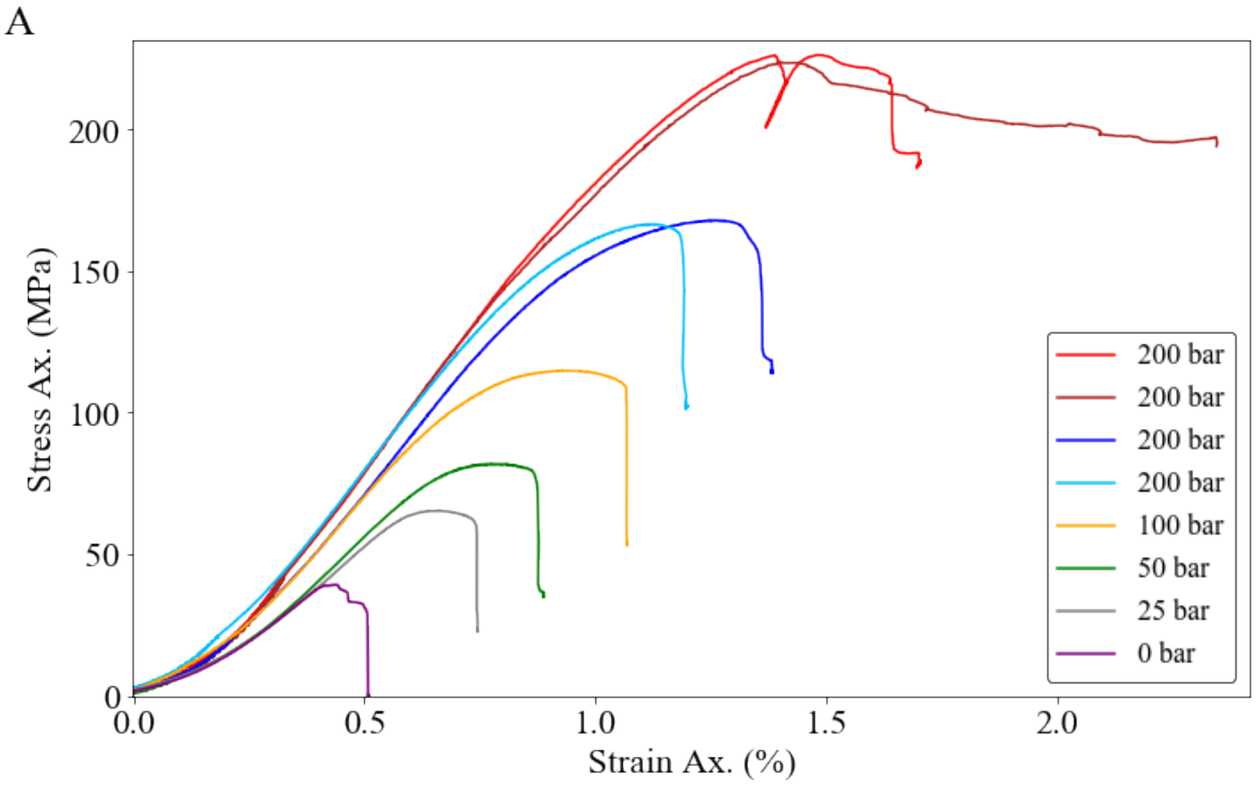
Stress Ax. (MPa)
Strain Ax. (%)
200 bar
200 bar
200 bar
200 bar
100 bar
50 bar
25 bar
0 bar

B

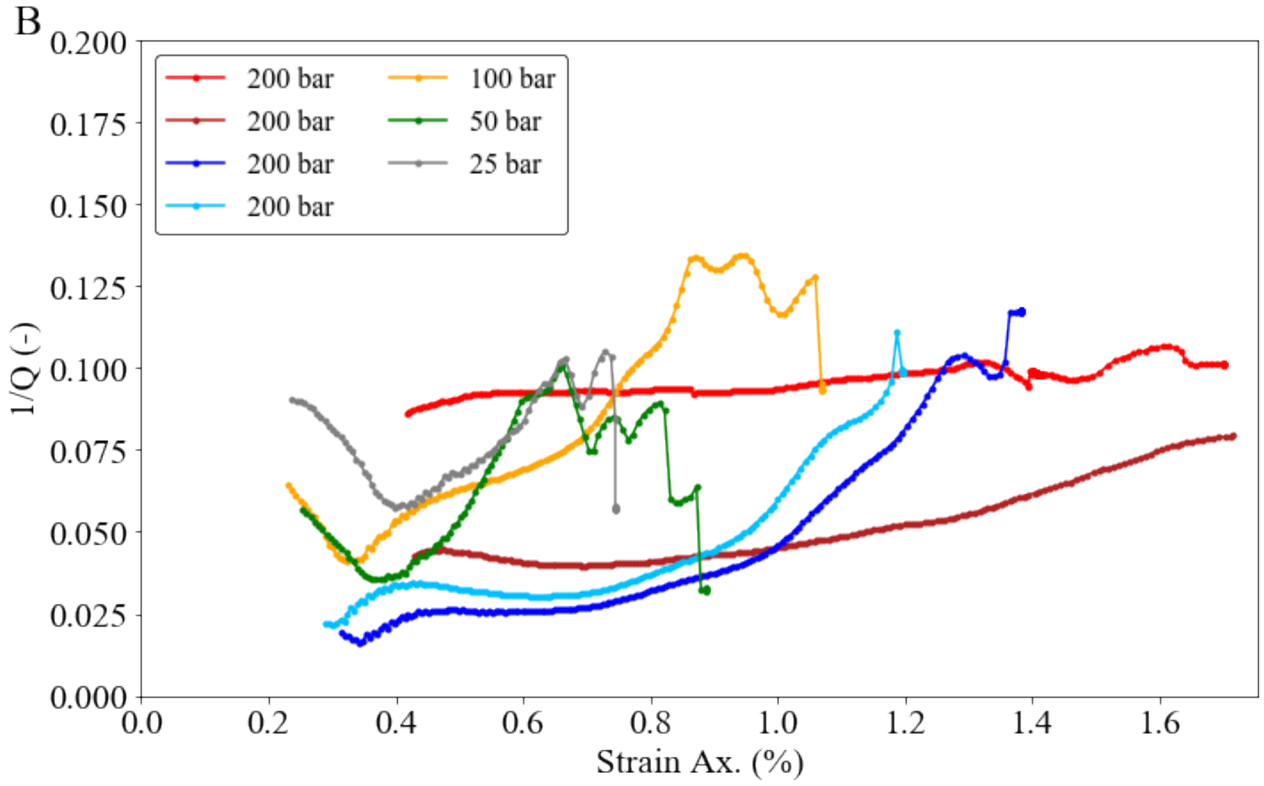
1/Q (-)
Strain Ax. (%)
200 bar
200 bar
200 bar
200 bar
100 bar
50 bar
25 bar

C

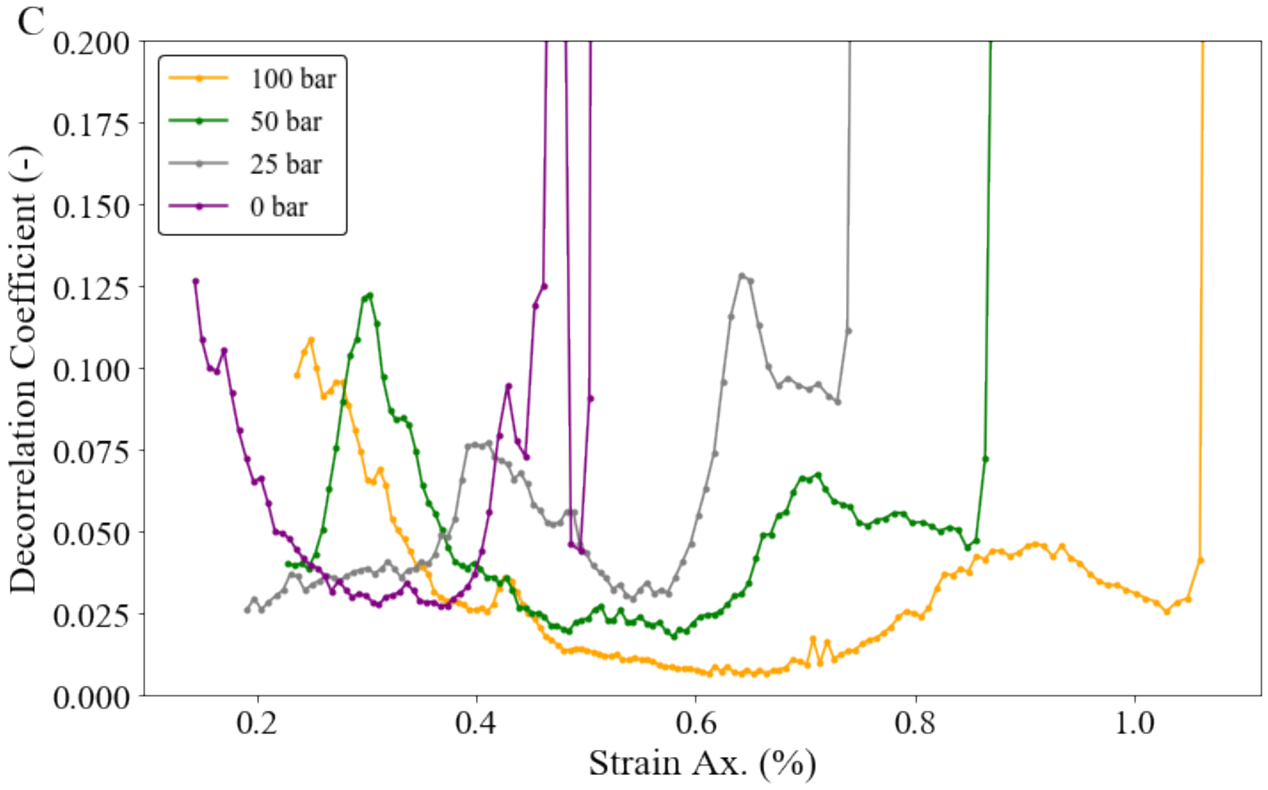
Decorrelation Coefficient (-)
Strain Ax. (%)
100 bar
50 bar
25 bar
0 bar

D

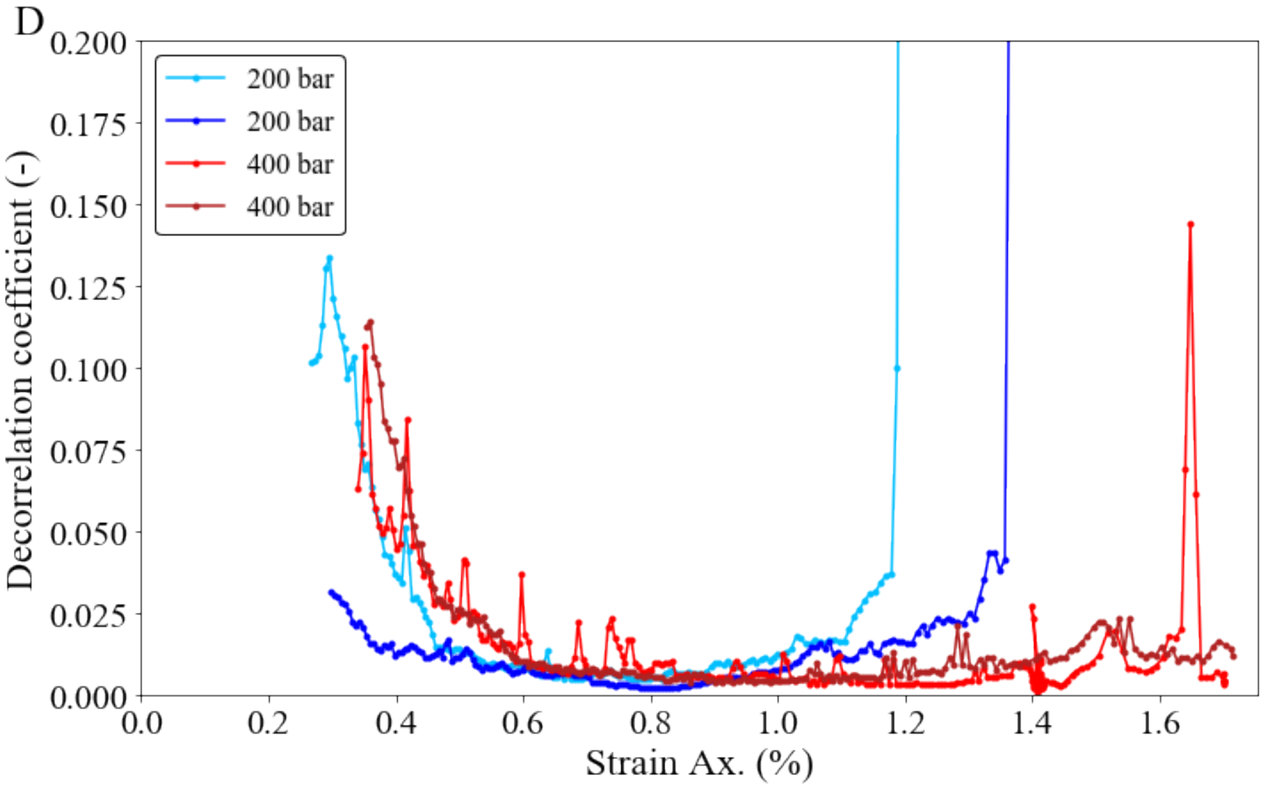
Decorrelation coefficient (-)
Strain Ax. (%)
200 bar
200 bar
400 bar
400 bar

E

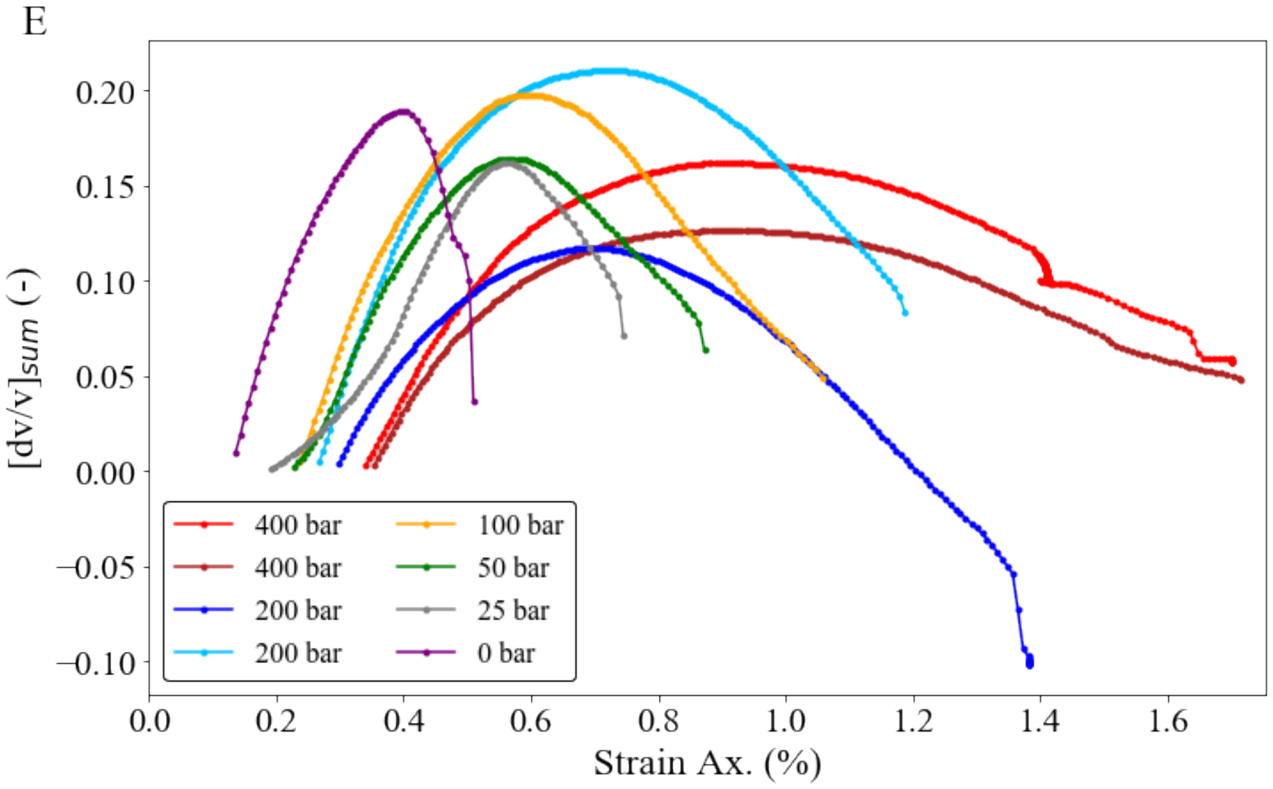
[dv/v]sum (-)
Strain Ax. (%)
400 bar
400 bar
200 bar
200 bar
100 bar
50 bar
25 bar
0 bar

F

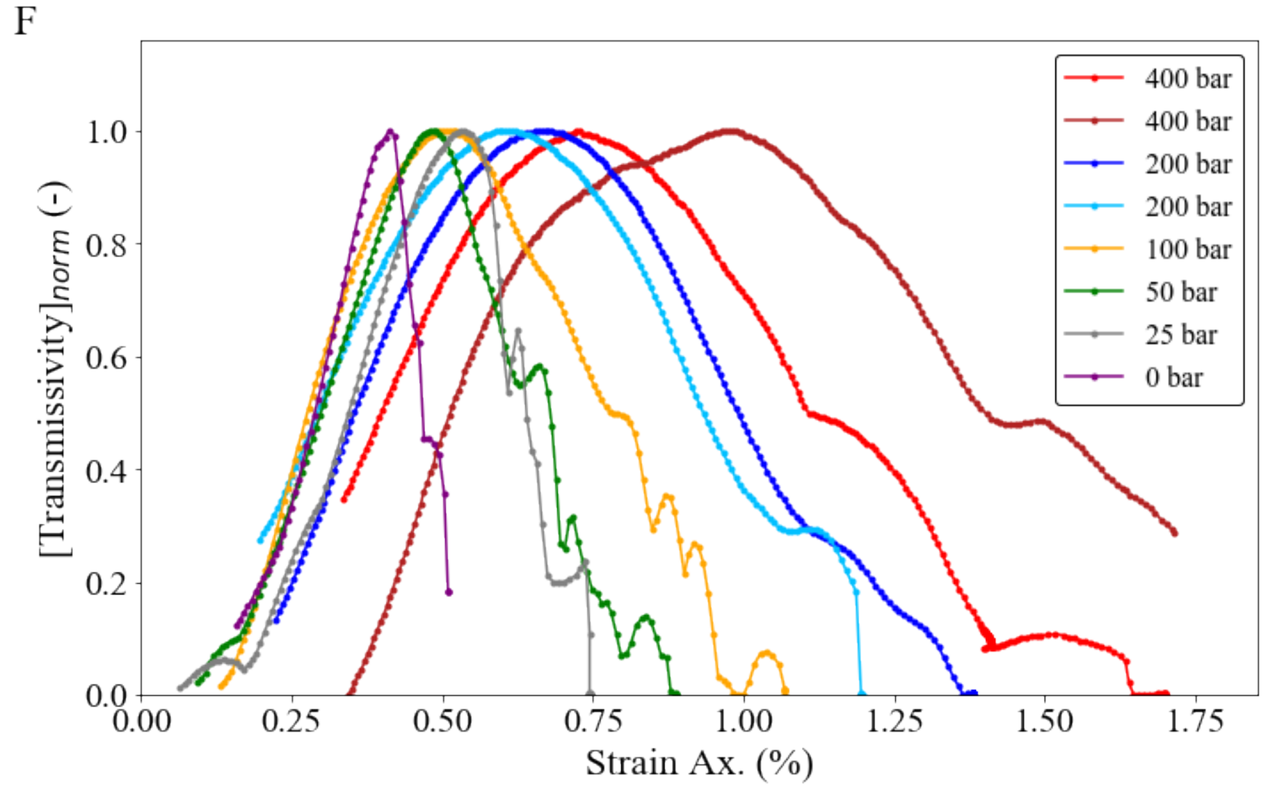
[Transmissivity]norm (-)
Strain Ax. (%)
400 bar
400 bar
200 bar
200 bar
100 bar
50 bar
25 bar
0 bar

G

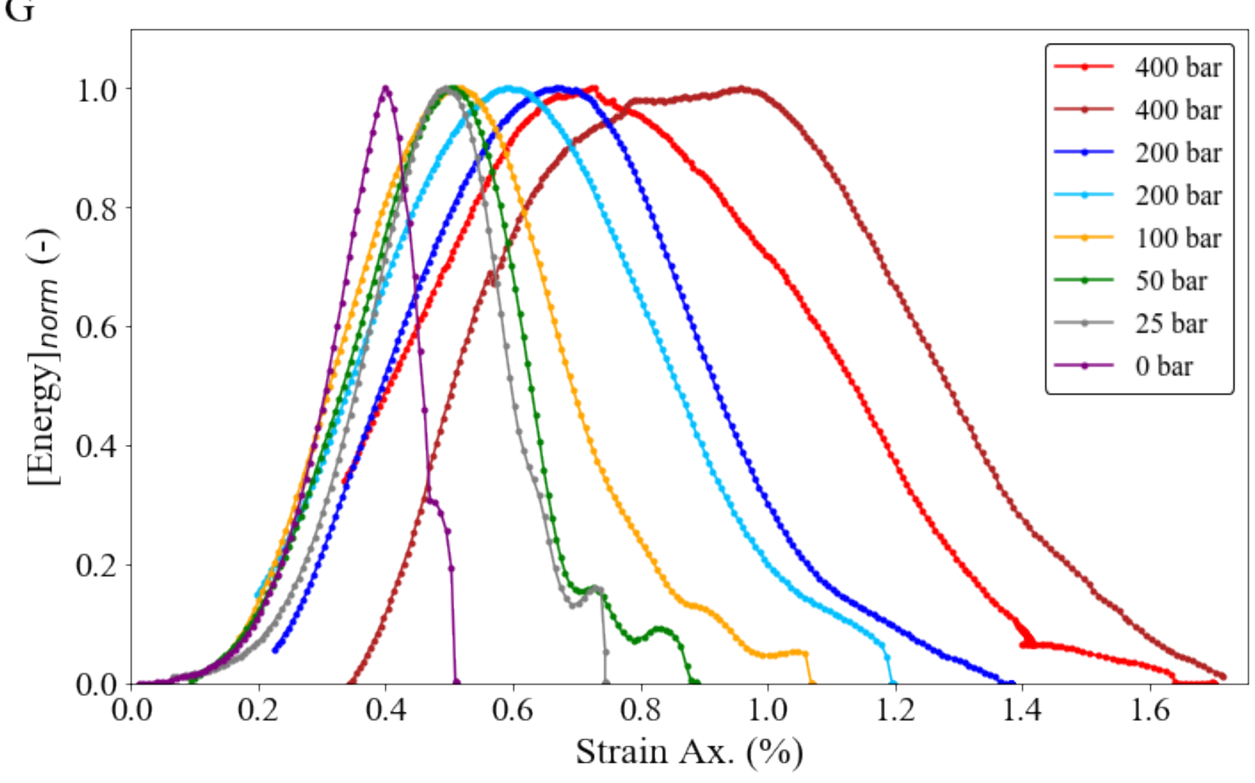
[Energy]norm (-)
Strain Ax. (%)
400 bar
400 bar
200 bar
200 bar
100 bar
50 bar
25 bar
0 bar

H

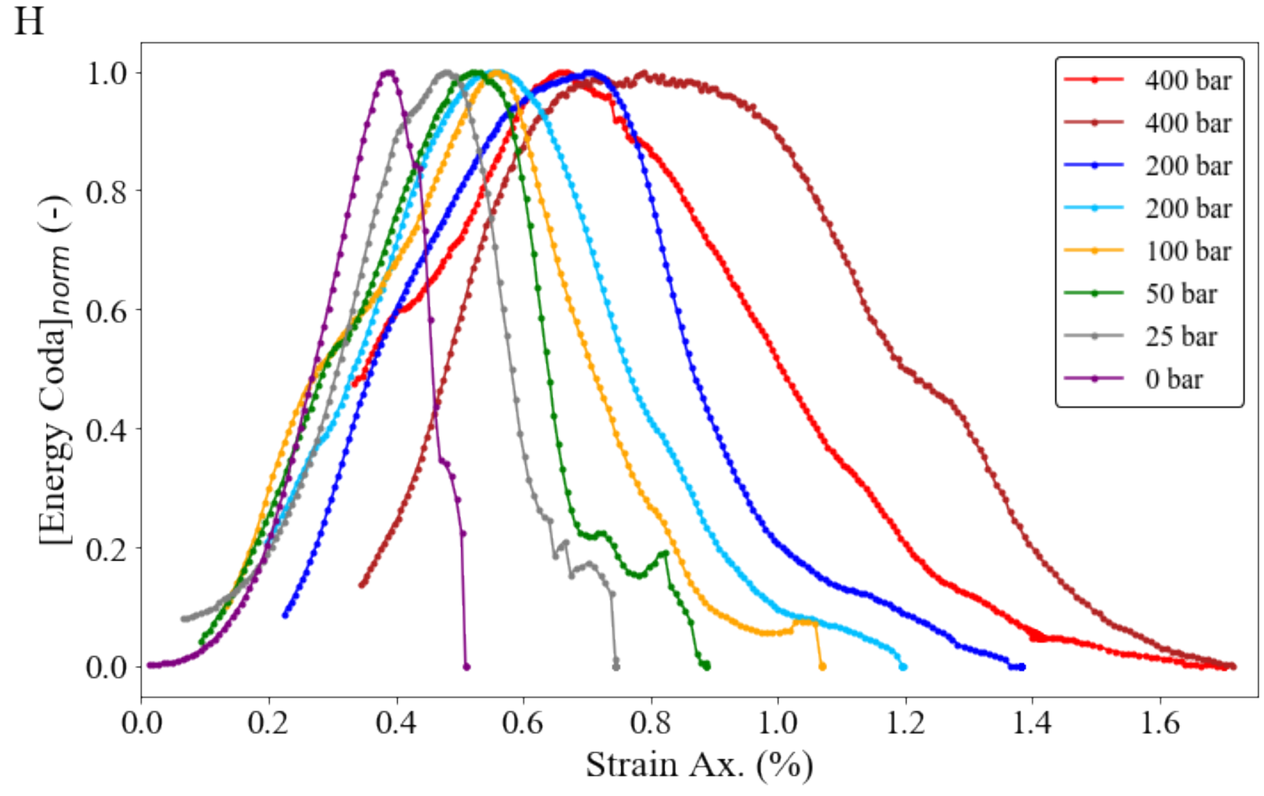
[Energy Coda]norm (-)
Strain Ax. (%)
400 bar
400 bar
200 bar
200 bar
100 bar
50 bar
25 bar
0 bar

Figure 4.

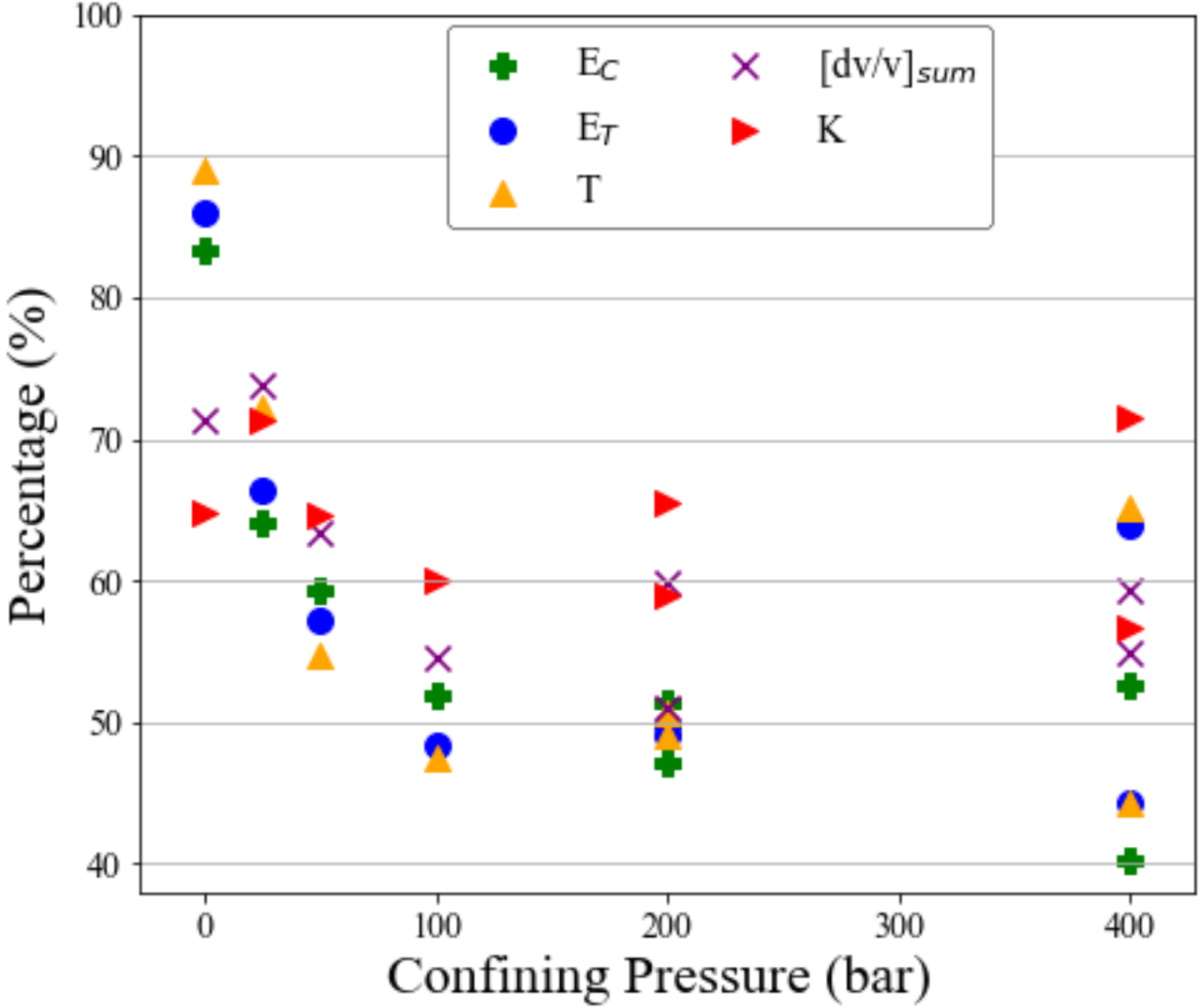
100
90
80
70
60
50
40
Percentage (%)
0
100
200
300
400
Confining Pressure (bar)
E_C
E_T
T
$[dv/v]_{sum}$
K

Figure 5.

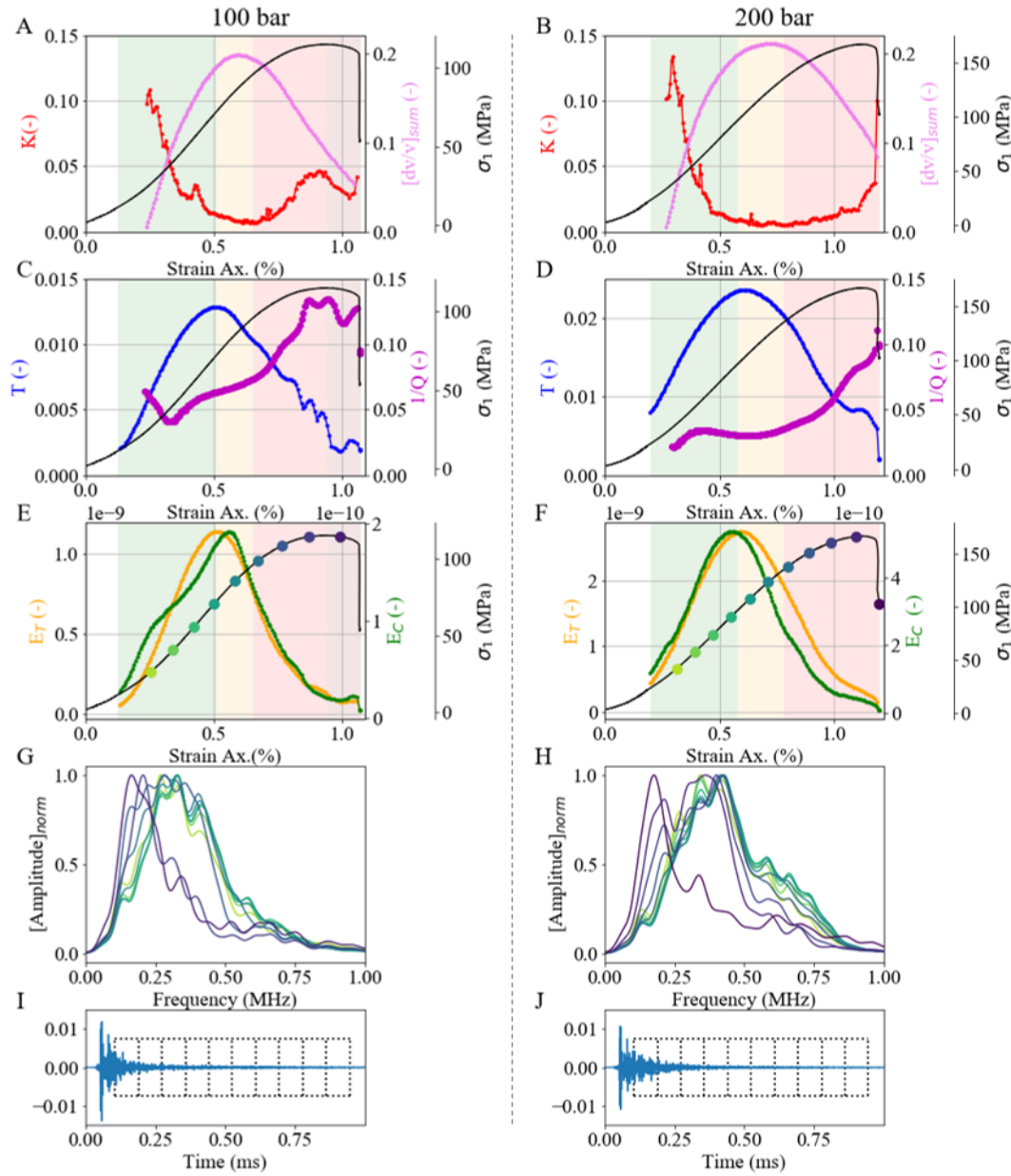
100 bar
200 bar
A
B
C
D
E
F
G
H
I
J
K(-)
[dv/v]sum (-)
σ1 (MPa)
Strain Ax. (%)
T (-)
1/Q (-)
1e−9
1e−10
ET (-)
EC (-)
[Amplitude]norm
Frequency (MHz)
Time (ms)

Figure 6.

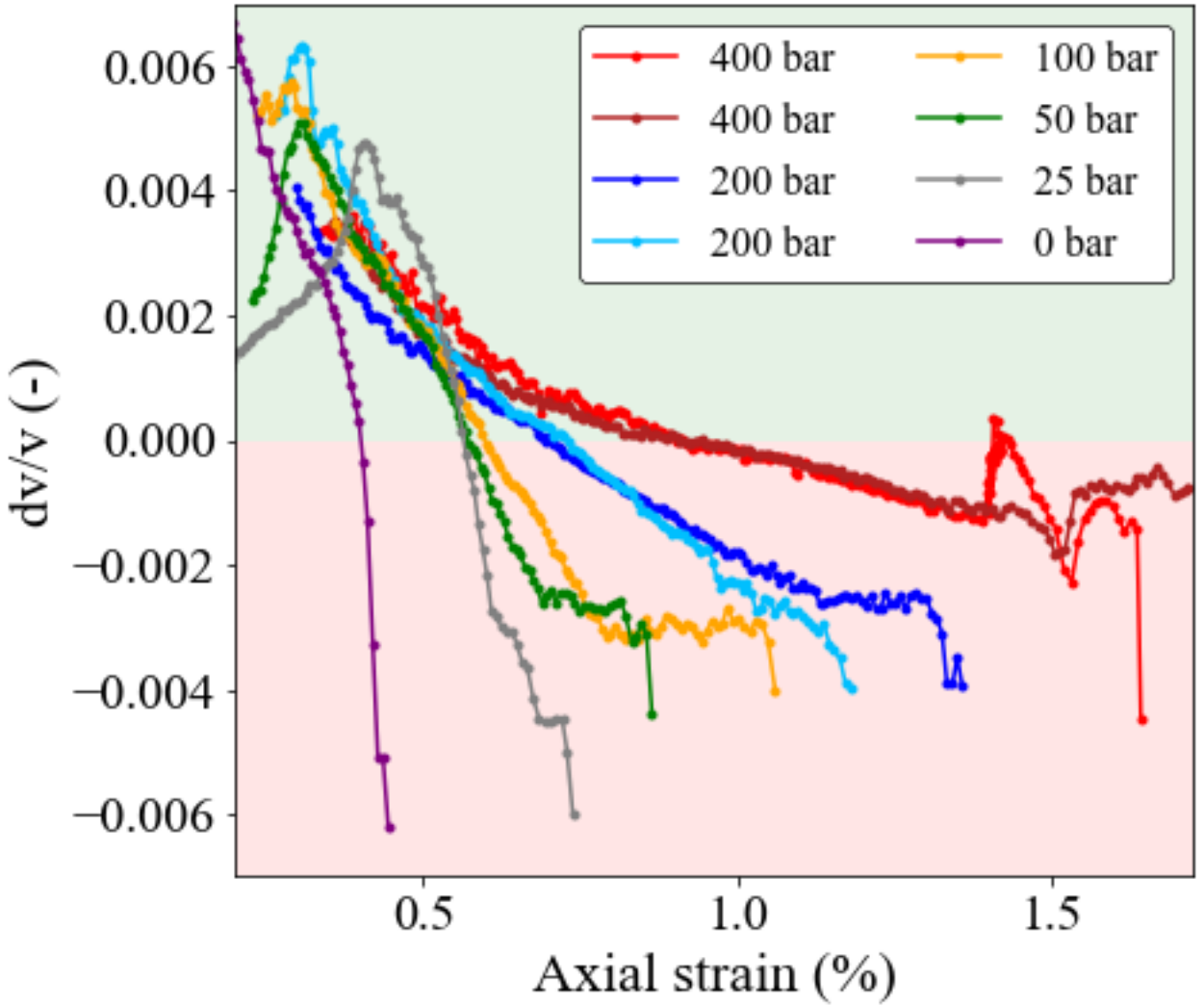
400 bar
400 bar
200 bar
200 bar
100 bar
50 bar
25 bar
0 bar
0.006
0.004
0.002
0.000
−0.002
−0.004
−0.006
dv/v (-)
0.5
1.0
1.5
Axial strain (%)

Figure 7.

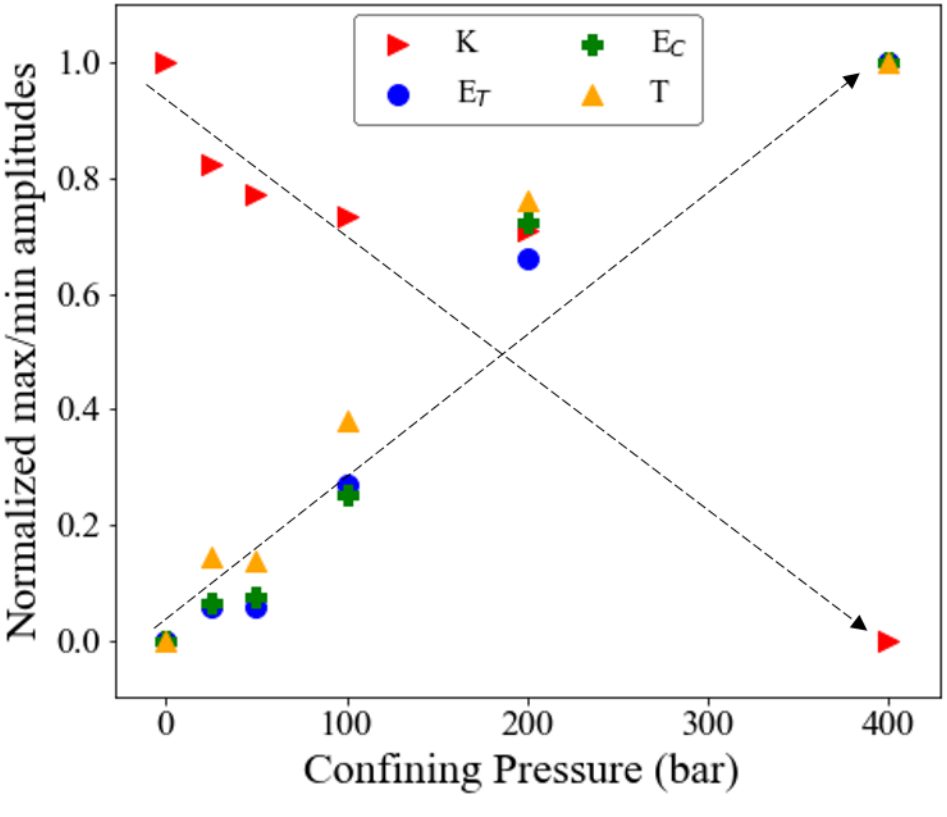
K
E_C
E_T
T
Normalized max/min amplitudes
1.0
0.8
0.6
0.4
0.2
0.0
0
100
200
300
400
Confining Pressure (bar)